

AE 460 Laboratory Report for Experiment 4

Experimental Design Laboratory

by

Amber Miller, William Boer, Musong Qin, Justin Magsino, Aden Litwiller

TA: Mateo Diaz

Section ABT, Group B, Wednesday 7:00pm-9:00pm

December 11, 2024

CubeSats have become a world-changing innovation in the space sector due to their cost effectiveness. So, there is a demand for a small, controllable CubeSat recovery vehicle capable of safely returning a 3U CubeSat payload from 70,000 feet to Earth. In this study, a 3D printed 1/4-scale model of a CubeSat recovery vehicle was designed, tested, and analyzed in a low-speed wind tunnel. The lift, drag, and pitching moment of the model were measured to assess the full-scale prototype's performance, including longitudinal static stability, stall characteristics, and performance across various speed ranges and angles of attack. The results show that the scaled-down model has a neutral point located 2.472 inches from the aft of the aircraft. The center of gravity of the scaled model is 3.3872 inches from the aft of the aircraft and 13.5488 inches from the aft end of the full scale-prototype. The lift-to-drag ratio of the aircraft with a 8.818 lb payload is 0.756, which resulted in a glide angle of 49.70 degrees. The neutral point of the model is 0.9152 inches behind the center of gravity, which makes the aircraft longitudinally stable. The results demonstrate that the proposed CubeSat recovery vehicle meets the requirements for controlled descent and recovery while maintaining robust aerodynamic performance.

I. Introduction

CubeSats are nanosatellites that revolutionized space exploration by being small, modular, and cost-effective to build and launch. First conceptualized in 1999, they use a standardized “1U” size of 3.94x3.94x4.33 inches, extendable to larger configurations such as 3U, 6U, and beyond. NASA Ames launched its first CubeSat, GeneSat, in December 2006 [2]. During the past decade, CubeSats have evolved from simple educational tools to versatile platforms for scientific investigations, technology demonstrations, and advanced mission concepts. Cubesats are stored inside containers located inside rockets, and they're ejected from the rockets into space by a spring mechanism attached to their dispensers. Cubesats usually conclude their missions by burning up as they enter the atmosphere after their orbits slowly decay [3]. As an alternative to letting the Cubesat disintegrate after the end of its mission, Spaceworks has developed re-entry capsules designed for efficient payload return. Their latest product, the RED-Data3, weighs less than 13.2 lbs and measures approximately 9.1 x 9.1 x 7.5 inches. This compact capsule is ideal for returning items such as Cubesats from Low Earth Orbit (LEO) to Earth's surface.[4]

CubeSats have provided universities and research institutions with affordable opportunities to design, build, and launch satellites. It provides students with valuable hands-on experience working with satellites, while enabling faculty to conduct additional research. One particularly impressive mission was the QuakeSat (3U CubeSat) mission. Launched in 2003, it successfully forecasted earthquakes. To do this, it carried a magnetometer housed in a 60 cm telescope for scanning and collecting global changes and fluctuations in Extremely-Low-Frequency-(ELF) electromagnetic waves,

which are believed to precede seismic activity [5]. Additionally, Cubesats can be used by militaries. Shari Feth, head of the Innovation, Science, and Technology directorate at MDA (Missile Defense Agency), stated, "The ability to use CubeSats for low-cost access to space is essential in maturing technologies for future applications in missile defense" [6].

On top of these uses, CubeSats are used by space agencies worldwide, including European Space Agency (ESA), Canadian Space Agency (CSA), NASA, and others. For example, the ESA uses Cubesats to carry out distributed multiple in-site measurements, such as obtaining simultaneous multi-point observations of the space environment (which might include the thermosphere, ionosphere, magnetosphere or charged particle flux) [7]. CubeSats are transforming the way space missions are conducted, enabling innovative approaches to exploration and experimentation. Entire constellations of CubeSats, flying in formation and working together, could make powerful observations analyzing everything from the nature of Europa's icy shell to the extremely low-frequency energy of far-away galactic nuclei and black holes. For more complex missions, swarms of CubeSats could be anchored by a single "hub" – a powerful central spacecraft that can handle complex computational tasks and data transmission back to Earth. Keeping each CubeSat simple and specialized will allow for more inexpensive deployment, greater reliability, and the incremental ability to add new CubeSats or replace malfunctioning units [8].

Cubesats transformed space missions by making them more accessible and cost-effective. However, there is still more potential to innovate, such as heterogeneous CubeSats-6G networks, software-defined networking, Internet of space things (IoST), hybrid architectures, ubiquitous coverage, and machine learning [5]. As of May 31, 2018, a total of 855 CubeSats had been launched [9], with projections indicating exponential growth in the years to come.

The authors have been tasked by a small company to design a small, controllable CubeSat recovery vehicle. The vehicle must be capable of recovering a 3U CubeSat payload (3.94 inches x 3.94 inches x 12.99 inches) and the vehicle must have a length of less than 33 inches and a wingspan of less than 24 inches. A large portion of the re-entry of the vehicle will be handled by a disposable capsule and the vehicle will be deployed at an altitude of 70,000 ft. and controlled all the way to the ground for landing. A 1/4-scale model of the actual design was built and 3D printed using Bambulab. Then, the model was tested in the Aerolab Low-Speed Wind Tunnel. The lift, drag, and pitching moment of the model were measured to assess the full-scale prototype's performance, including longitudinal static stability, stall characteristics, and performance across various speed ranges and angles of attack.

II. Theory and Analysis

A. Reynolds Number Determination

The Reynolds Number of each test is calculated according to:

$$Re = \frac{\rho V_{\infty} \bar{c}}{\mu} \quad (1)$$

where ρ is density, V_{infty} is the free-stream velocity, μ is dynamic viscosity, and \bar{c} is the mean aerodynamic chord. \bar{c} is found with the equation:

$$\lambda = \frac{C_{tip}}{C_{root}} \quad (2a)$$

$$\bar{c} = \frac{2}{3} C_{root} \frac{1 + \lambda + \lambda^2}{1 + \lambda} \quad (2b)$$

where λ is the taper ratio, C_{root} is the root chord, and C_{tip} is the tip chord.

B. Lift and Drag Determination

The sting balance measures net normal and axial force acting on the model. In other words, the sting balance is not zeroed for the model weight. In the model frame, the weight acts in different directions depending on the angle of attack, as shown in the free body diagram in Figure 1.

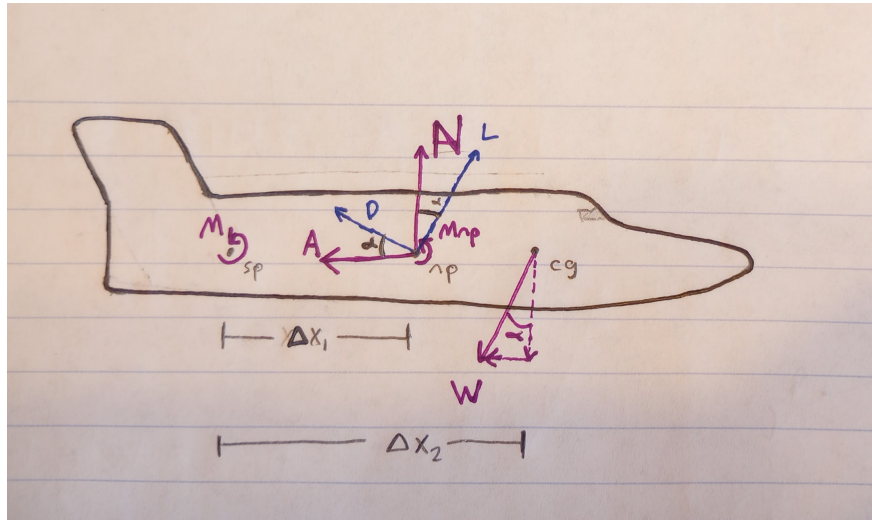


Fig. 1 Caption

Therefore, the total normal and axial forces are given by:

$$N_{total} = N_{measured} + W \cos(\alpha) \quad (3a)$$

$$A_{total} = A_{measured} - W \sin(\alpha) \quad (3b)$$

where $N_{measured}$ and $A_{measured}$ are the forces measured by the sting balance, N_{total} and A_{total} are the total normal and axial forces acting on the model, and W is the magnitude of the weight of the model.

Next, the total normal and axial force can be used to find lift and drag according to:

$$L = N_{total}\cos(\alpha) - A_{total}\sin(\alpha) \quad (4a)$$

$$D = N_{total}\sin(\alpha) + A_{total}\cos(\alpha) \quad (4b)$$

Finally, these are nondimensionalized to get the lift and drag coefficients:

$$C_L = \frac{L}{\frac{1}{2}\rho V_\infty^2 S} \quad (5a)$$

$$C_D = \frac{D}{\frac{1}{2}\rho V_\infty^2 S} \quad (5b)$$

where V_∞ is free-stream velocity, ρ is the density in the wind-tunnel, and S is the planform area.

C. Neutral Point Location Determination

To find the neutral point, which is the point where the pitching moment is constant with relation to angle-of-attack, a guess and check method was employed.

First, using the free body diagram in Figure 1, the measured moment measured by the sting balance can be defined by:

$$M_{measured} = M_{np} + N_{total}\Delta x_1 - W\Delta x_2 \quad (6)$$

where Δx_1 is the distance from the sting balance tip to the neutrap point, Δx_2 is the distance from the sting balance tip to the center of gravity, and M_{np} is the moment about the neutral point. Next, Equation 6 can be solved in terms of M_{np} to get:

$$M_{np} = M_{measured} - N_{total}\Delta x_1 + W\Delta x_2 \quad (7)$$

Then, the values $\Delta x_1 = x_{np} - x_{sp}$ and $\Delta x_2 = x_{cg} - x_{sp}$ can be subbed into Equation 7, resulting in:

$$M_{np} = M_{measured} - N_{total}(x_{np} - x_{sp}) + W(x_{cg} - x_{sp}) \quad (8)$$

where x_{sp} is the location of the sting point tip, x_{cg} is the location of the center of gravity, and x_{np} is the location of the neutral point.

By guessing different values for x_{np} and then viewing the shape of the plot of M_{np} versus α , x_{np} can be determined

as the value where the trend-line of that plot is flat.

Finally, once the neutral point is found, the moment about the neutral point can be found as the mean value of the M_{np} versus α plot. Then, the moment coefficient can be found as:

$$C_{M,np} = \frac{M_{np}}{\frac{1}{2}\rho V_{\infty}^2 Sc} \quad (9)$$

where \bar{c} is the mean aerodynamic chord.

III. Apparatus

The experimental setup involves a test model that's 3D printed using the Bambu X1 Carbon 3D Printer. The model is mounted to the sting balance using a screw which is integrated with the Model Positioning System inside the Aerolab Low-Speed Wind Tunnel. The angle of attack of the model is verified to be 0 degrees. The atmospheric pressure and ambient temperature data for the runs for the day of the test and each run setting is recorded into the Labview program. The wind tunnel is set to various velocity that matches the desired Reynold numbers. For each Reynolds number tested, the angle of attack of the model is changed from -6 degrees to 24 degrees with increments of 2 degrees. The Sting balance uses strain gauges to capture normal force, axial force, and pitching moment. These measurements are sent to the Labview program where they are processed and recorded.

Table 1 Major Laboratory Equipment

No.	Item	Size/Range/Capacity	Accuracy	Use in Experiment
1	Aerolab Low-Speed Wind Tunnel	12"x12"x24" test section, 10-hp motor, 10-145+ mph operational range [1]	Turbulence level - Less than 0.2% [1]	Create a controlled environment which simulates varying levels of airflow to collect data
2	Omega PX653 Pressure Transmitter	static pressure: 0-±10" inches of water [1]	± 0.25% full scale [1]	Measures the difference between the static pressure measured by the static pressure ring and the atmospheric pressure
3	3-Component Sting Balance	20 lbs maximum normal force, 9 lbs maximum axial force, 40 inch-lbs maximum pitching moment [1]	5% in force and moment measurements [1]	It uses strain gauges to measure the normal and axial force and pitching moment about the balance center located 1.12" from the end of the sensing tip
4	Model Positioning System	-10 to 35 ° [1]	± 0.2° [1]	Used to change the angle of attack of the model using the knob located at the bottom.
5	Bambu X1 Carbon 3D Printer	10.08×10.08×10.08inches building envelope [1]	Precision within 3.150e-4 inches [1]	Used to print the model

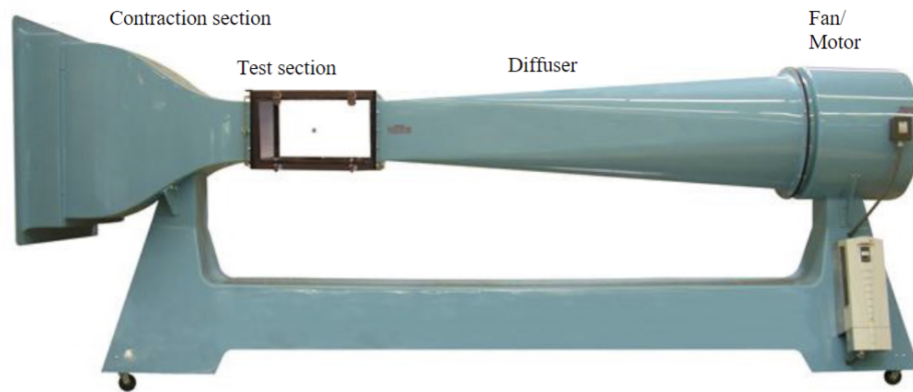


Fig. 2 Aerolab low-speed wind tunnel.



Fig. 3 Fan Speed Controller and Pressure Transducer.

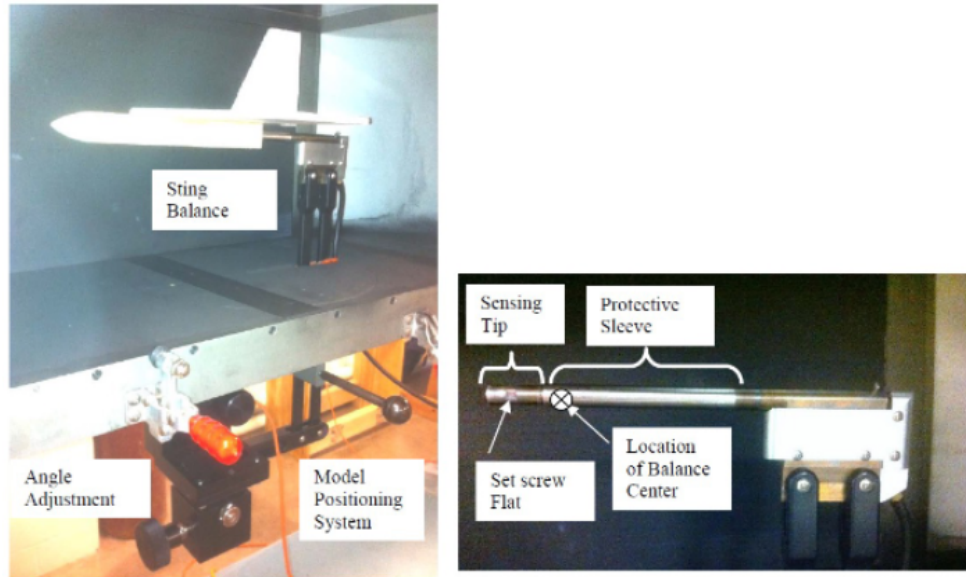


Fig. 4 Sting Balance and Model Positioning



Fig. 5 Bambu Lab X1 Carbon 3D printer.

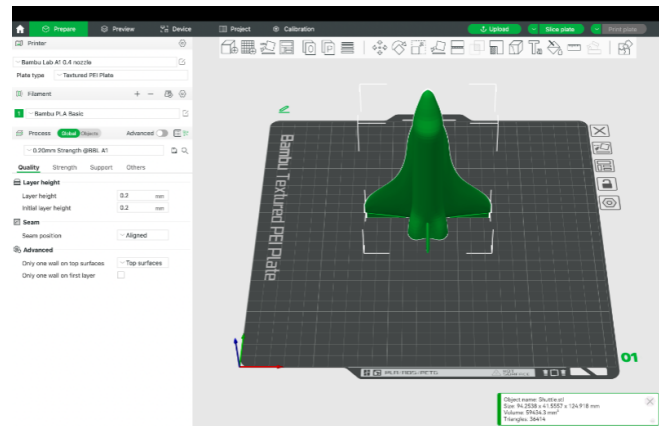


Fig. 6 Bambu Studio program for rendering the layers of the 3D printed model.

IV. Procedure

The following steps outline the procedure for the experiment. Words denoted in **bold** (e.g., [Start]) indicate physical buttons on the frequency control keypad, computer keyboard, or radio buttons on the computer screen. Radio buttons are activated by pressing the left mouse button while the cursor is placed over the radio button.

A. 4.1 Prepare the Equipment

- 1) Take out and prepare the space shuttle model for mounting.

- 2) Align the opening at the back of the space shuttle model with the cylindrical mount to attach it.
- 3) Insert the set screw into the hole, ensuring it is tightened on the flats on the sensing tip to secure the model to the sting balance. Make sure not to over-tighten the screw to prevent damage to the unit.
- 4) Ensure the space shuttle model is securely attached to the cylindrical mount before proceeding to the next step.

B. 4.2 Data Acquisition

- 1) Open the **LabVIEW** program on the computer.
- 2) Under the **Inputs Value** block, enter the atmospheric pressure and ambient temperature data for the runs for the day of the test and each run setting. Record these values on the datasheet as well.
- 3) Verify that the space shuttle model is at zero angle of attack and that the RPM is set to zero on the frequency control pad.
- 4) Adjust the tunnel speed input frequency with the up and down arrow buttons on the keypad, setting the frequency so that the freestream velocity in the wind tunnel is equal to 50 ft/s.
- 5) Adjust the angle of attack of the space shuttle model by rotating the sting balance knob to the first angle of -6 degrees. Change the speed frequency input to obtain a value close to the desired velocity. Ensure that the sting balance reading does not exceed 20 lbs for the normal force, 9 lbs for the axial force, and 40 inch-lbs for the pitching moment.
- 6) Adjust the tunnel speed frequency until the freestream velocity is equal to 50 ft/s again.
- 7) Once the desired velocity is obtained, press the **[Record Data Point]** button to record all the model pressure measurements.
- 8) On the datasheet, record the normal force, axial force, pitching moment, the differential pressure from the Omega transmitter (ΔP [dpsi]), freestream dynamic pressure, velocity, and Reynolds number of the recorded point.
- 9) Repeat steps 4–8, starting at -6° and increasing the angle of attack by 2 degrees until the apparatus limit.
- 10) After the last angle of attack is recorded, set the angle of attack back to zero.
- 11) Adjust the tunnel speed input frequency with the up and down arrow buttons on the keypad so that the freestream velocity in the wind tunnel is 30 ft/s.
- 12) Once the desired velocity is obtained, press the **[Record Data Point]** button to record all the model pressure measurements.
- 13) On the datasheet, record the normal force, axial force, pitching moment, the differential pressure from the Omega transmitter (ΔP [dpsi]), average dynamic pressure (Average Rake q [dpsi]), freestream dynamic pressure, velocity, and Reynolds number of the recorded point.
- 14) Repeat steps 11–13, starting at 15 ft/s and increasing by increments of 10 ft/s until 85 ft/s is reached.
- 15) After the last data point is recorded, press the **[Save All Data]** button and save the file in your EWS Home

directory.

- 16) Shut down the tunnel by pressing the [STOP] button.

V. Results and Discussion

A. Question 1

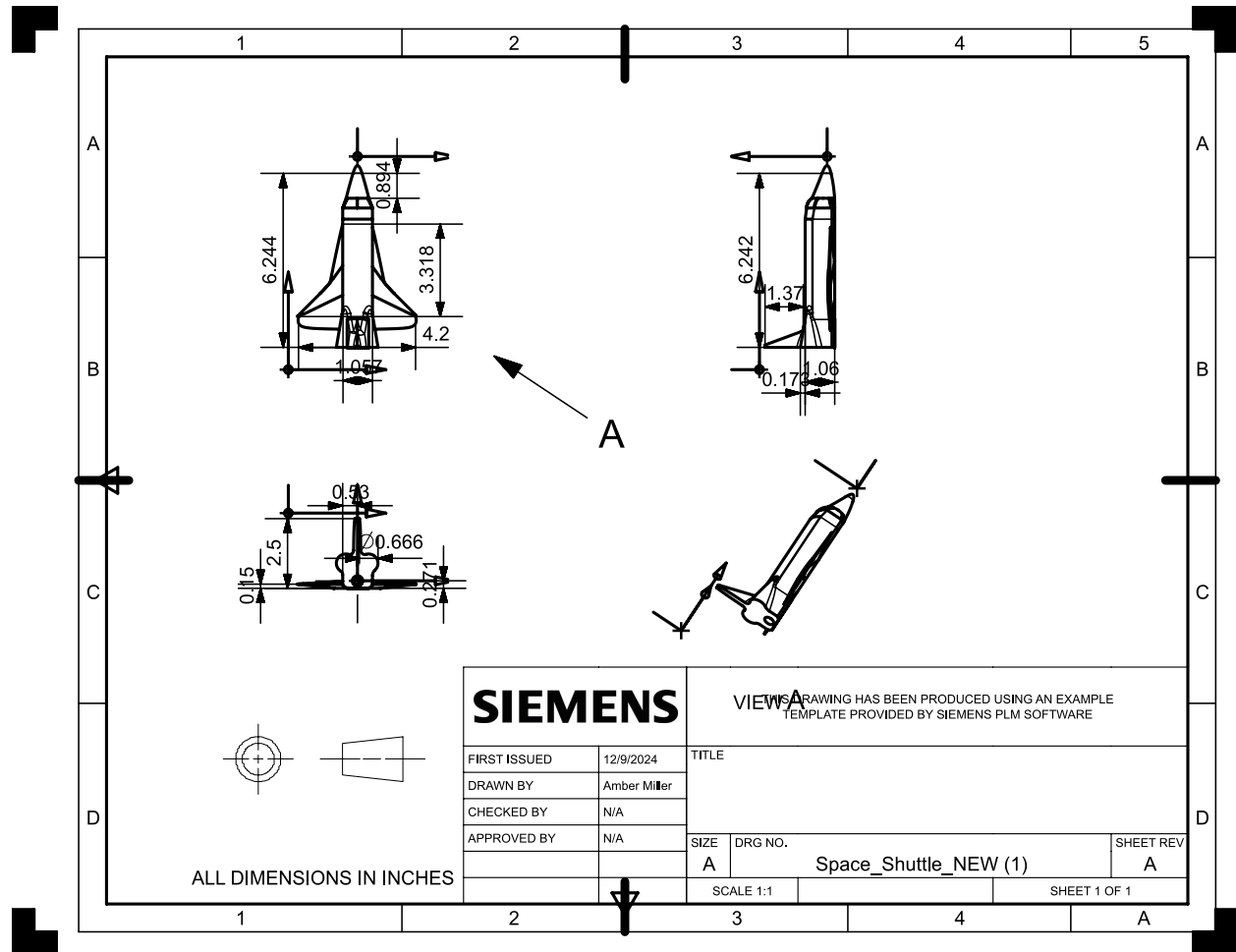


Fig. 7 Space Shuttle 3-View

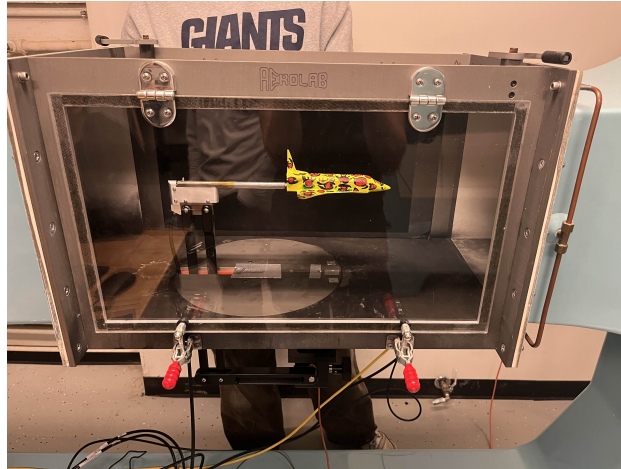


Fig. 8 Space Shuttle View In Wind Tunnel

Planform Area	31.775 in^2
Mean Aerodynamic Chord	3.27 in
Length	6.244
Wing Span	4.267 in

Table 2 Generic Dimensions

The general dimensions for this model were derived to be as close to a scaled down version of the real space shuttle as possible. As a result, the 3-view of the space shuttle as shown below, with preliminary dimensions, was used as a template to design the actual model. The wing for this model is derived from the space shuttle design, which utilizes a novel delta wing with no reference airfoil. As a result, in the model of the wing the thickness was modeled to look like an ellipse.

B. Question 2

To simulate an expected performance of the actual model, Ansys Fluent was used to analyze the performance of the wing at 0° angle of attack and a freestream velocity of 88.7 m/s. As seen in the figure 9, the wing performs well with defined velocity streamlines going over the wing and generating lift without much separation of flow or turbulence. The velocity gradients below the wing are smaller than those found above the wing, showing lift being generated in accordance with Bernoulli's principle. Additionally, a distinct wake downstream from the wing can be observed which demonstrates high aerodynamic efficiency and low drag. Through these contours, it shows the effectivity of the wing designed even in the expected flight conditions as it is able to generate enough lift while also decreasing drag which is optimal for the vehicle when carrying its payload and actual airframe weight.

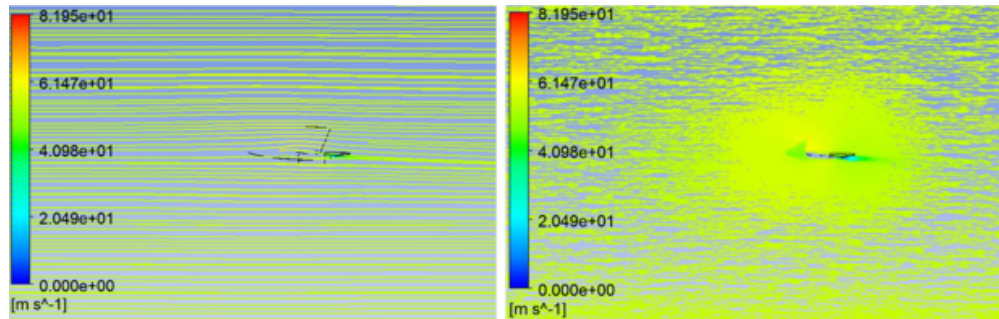


Fig. 9 CFD analysis over the wing in Ansys Fluent

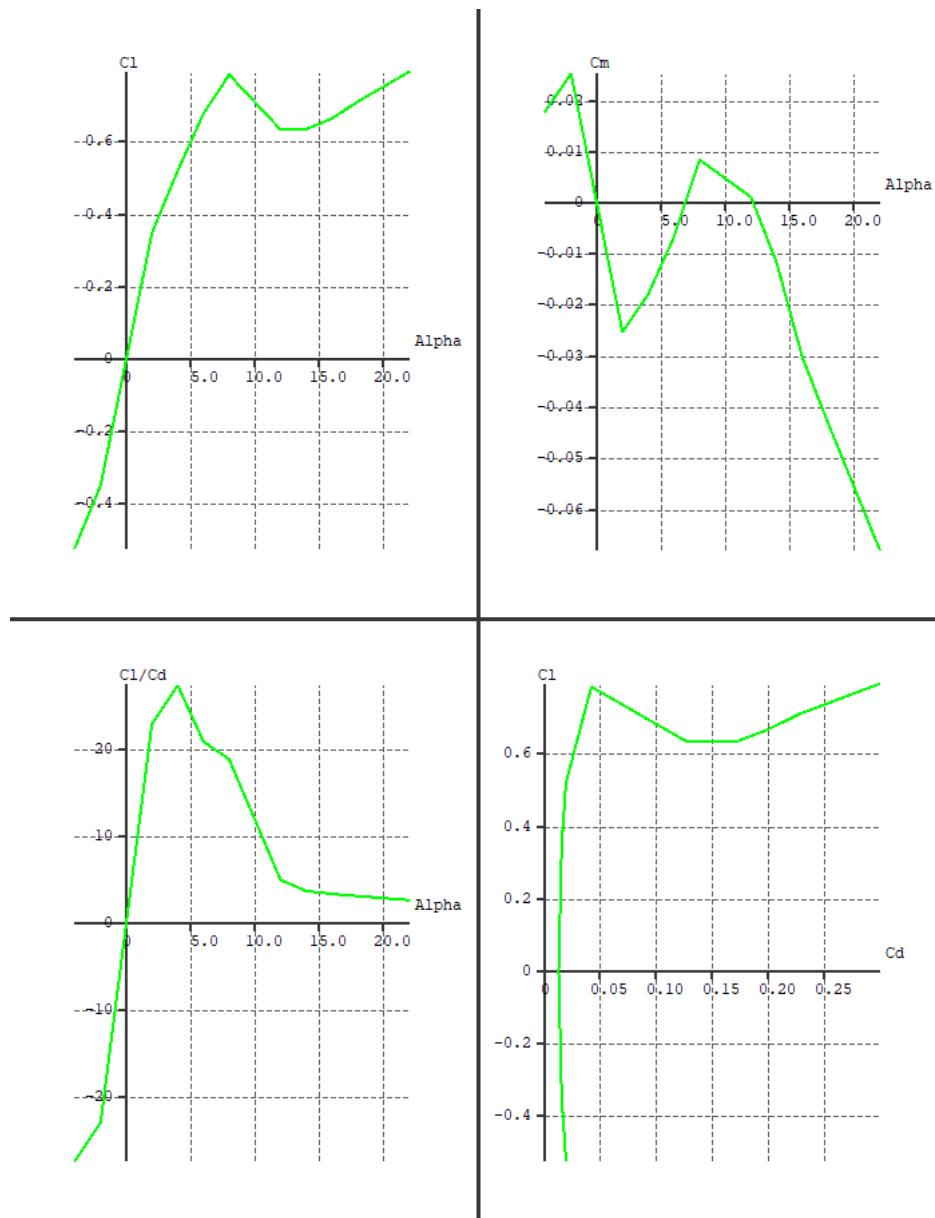


Fig. 10 Varying graphs showing airfoil performance in XFLR5 simulations

Further analysis on the airfoil can be shown in Figure 10 using XFLR5. Through this figure, the graphs of CL , C_m , and CL/CD vs angle of attack as well as CL vs CD can be viewed. To simulate expected flight conditions, the airfoil was run at a Reynolds number of 148000 which was the maximum Reynolds number run in the wind tunnel. From these graphs, it can be seen that the coefficient of lift trends upward, only stalling a little around 8° before trending upward once more. This further supports how the design of the wing will perform well in the expected conditions at 70,000 ft. The airfoil analysis also shows a high CL/CD ratio until around 4° after which it begins to decrease, showing the wing's aerodynamic efficiency producing more lift than drag before the angle of attack causes an increase in drag.

C. Moments and Forces Measurement Data

Figure 3 shows the measured values for a Reynolds number of $5.51e4$.

Angle of Attack (deg)	Axial Force (lbf)	Normal Force (lbf)	Pitching Moment (in-lbf)
-6.0	-0.00236	-0.0977	-0.0771
-4.1	0.00307	-0.0885	-0.0603
-2.1	0.0224	-0.0820	-0.0400
-0.1	0.0282	-0.0726	-0.0206
2.0	0.0396	-0.0633	-0.0045
4.0	0.0496	-0.0552	0.0141
6.1	0.0584	-0.0465	0.0336
7.9	0.0791	-0.0375	0.0537
10.0	0.0936	-0.0296	0.0783
12.1	0.1101	-0.0164	0.1034
14.0	0.1182	-0.0088	0.1212
16.0	0.1346	-0.0002	0.1474
18.0	0.1447	0.0099	0.1719
19.9	0.1592	0.0205	0.1970
22.0	0.1694	0.0315	0.2260
24.0	0.1641	0.0423	0.2520

Table 3 Axial Force, Normal Force, and Pitching Moment on Recovery Vehicle Scale Model for $Re = 5.51e4$

Table 4 shows these values for a Reynolds number of 8.93e4.

Angle of Attack (Lbf)	Axial Force (Lbf)	Normal Force (Lbf)	Pitching Moment (in-Lbf)
-6.0	0.0146	-0.105	-0.160
-4.0	0.0338	-0.0927	-0.122
-1.9	0.0457	-0.0788	-0.075
0.0	0.0538	-0.0604	-0.029
2.0	0.0636	-0.0443	0.013
4.0	0.0787	-0.0271	0.060
6.1	0.0870	-0.0105	0.103
7.9	0.112	0.00633	0.154
10.1	0.131	0.0241	0.208
11.9	0.137	0.0379	0.244
14.0	0.146	0.0584	0.299
16.0	0.162	0.0763	0.356
18.0	0.171	0.100	0.415
20.0	0.182	0.116	0.464
21.9	0.189	0.144	0.533
24.1	0.198	0.158	0.589
26.0	0.195	0.174	0.632
28.1	0.210	0.190	0.668

Table 4 Axial Force, Normal Force, and Pitching Moment on Recovery Vehicle Scale Model for $R_e = 8.93e4$

Table 4

Angle of Attack (lbf)	Axial Force (lbf)	Normal Force (lbf)	Pitching Moment (in-lbf)
-6.1	0.0556	-0.195	-0.327
-4.1	0.0636	-0.168	-0.241
-2.0	0.0877	-0.137	-0.157
-0.0	0.0945	-0.107	-0.081
2.0	0.107	-0.074	0.008
4.0	0.117	-0.045	0.087
6.0	0.130	-0.011	0.183
7.9	0.143	0.023	0.272
10.0	0.149	0.055	0.366
12.1	0.168	0.085	0.449
14.0	0.179	0.125	0.562
16.0	0.194	0.159	0.656
18.0	0.197	0.197	0.751
19.9	0.187	0.245	0.879
21.9	0.214	0.283	0.978
23.9	0.218	0.302	1.05

Table 5 Axial Force, Normal Force, and Pitching Moment on Recovery Vehicle Scale Model for $R_e = 1.22e5$

Table 5 shows these values for a Reynolds number of 1.22e5.

These values for Reynolds number were chosen because they corresponds the the range of design velocities for the full-scale prototype, as demonstrated in the Subsection "Full-Scale Prototype Equivalent Mach Numbers."

D. Lift, Drag, and Moment Coefficients

The neutral point of the aircraft model was determined by iteratively solving a moment equilibrium equation taking into account the moment measured at the sting balance, the moment caused by the normal force as well as the weight of the aircraft acting through its center of gravity.

$$M_{NP} = M_{Sting} + F_N \cdot (X_{NP} - X_{Sting}) - m \cdot g \cdot \cos(\alpha) \cdot (X_{CG} - X_{Sting}) \quad (10)$$

Where M_{NP} is the moment about the neutral point, M_{Sting} is the moment about the sting balance, F_N is the normal force and X_{CG} , X_{Sting} & X_{NP} being the distances from a chosen reference point (tail of aircraft) to the center of gravity, sting balance measurement location and neutral point respectively. It should be noted that the data for the moment about the sting balance and the normal force has already been adjusted at this point such that any contributions of weight have been removed. The Neutral point was found by plotting M_{NP} against the angle of attack, α for different input values of X_{NP} . Because the rate of change of moment coefficient with respect to angle of attack is zero at the neutral point, it can be concluded that an approximate value for the neutral point is found when the trendline for the plotted points shows zero gradient. Subsequently the distance from the aft of the aircraft to the neutral point is 2.472 inches. The moment coefficient for moments around the neutral point against angle of attack is depicted in Figure 11.

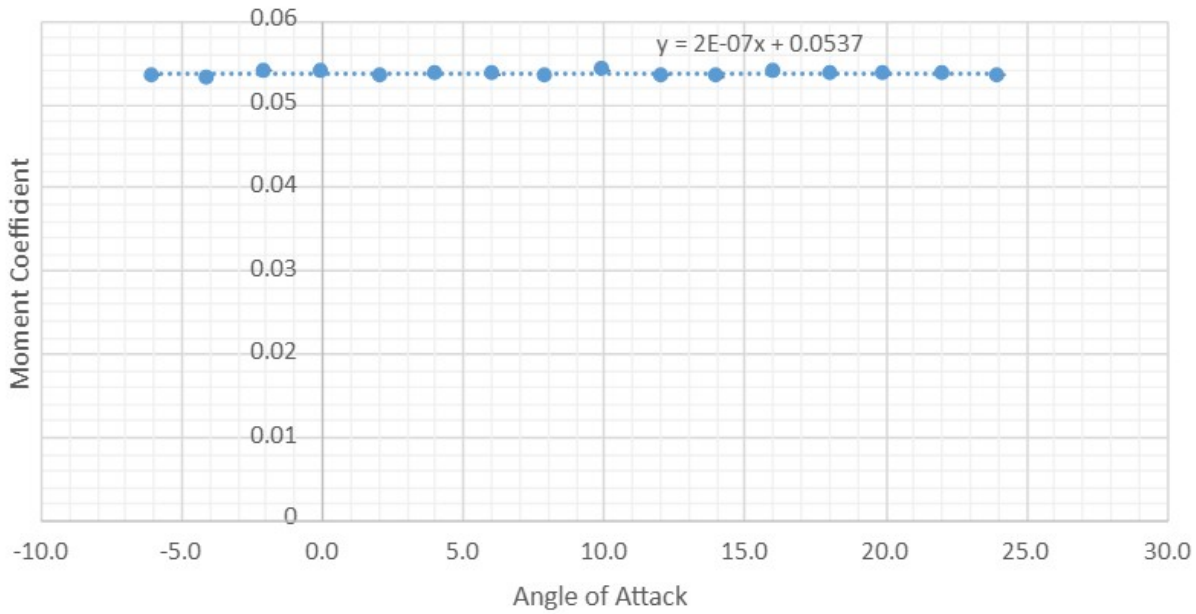


Fig. 11 Moment Coefficient with increasing Angle of Attack about the neutral point of the aircraft model

Data collected from sting balance measurements was used when calculating lift, drag and moment coefficients for the aircraft. These measurements did not take into account the aircraft's weight and therefore the data had to be adjusted before the coefficient calculations were carried out. The following corrections were made to convert the raw data into three separate measurements containing only axial force, normal force and moment:

$$F_A = A - m \cdot g \cdot \sin(\alpha) \quad (11)$$

$$F_N = N + m \cdot g \cdot \cos(\alpha) \quad (12)$$

$$M_{Sting} = M_{Reading} + m \cdot g \cdot \cos(\alpha) \cdot (X_{CG} - X_{Sting}) \quad (13)$$

Where A , N and $M_{Reading}$ are the raw data measurements obtained from the sting balance apparatus. Once this was completed the lift and drag forces were computed by decomposing the normal and axial forces using the aircraft's angle of attack.

$$L = F_N \cdot \cos(\alpha) - F_A \cdot \sin(\alpha) \quad (14)$$

$$D = F_A \cdot \cos(\alpha) + F_N \cdot \sin(\alpha) \quad (15)$$

Once these values were calculated, the lift and drag coefficients were computed and plotted. These calculations are demonstrated in the appendix. These plots can be seen in Figure 12 and Figure 13.

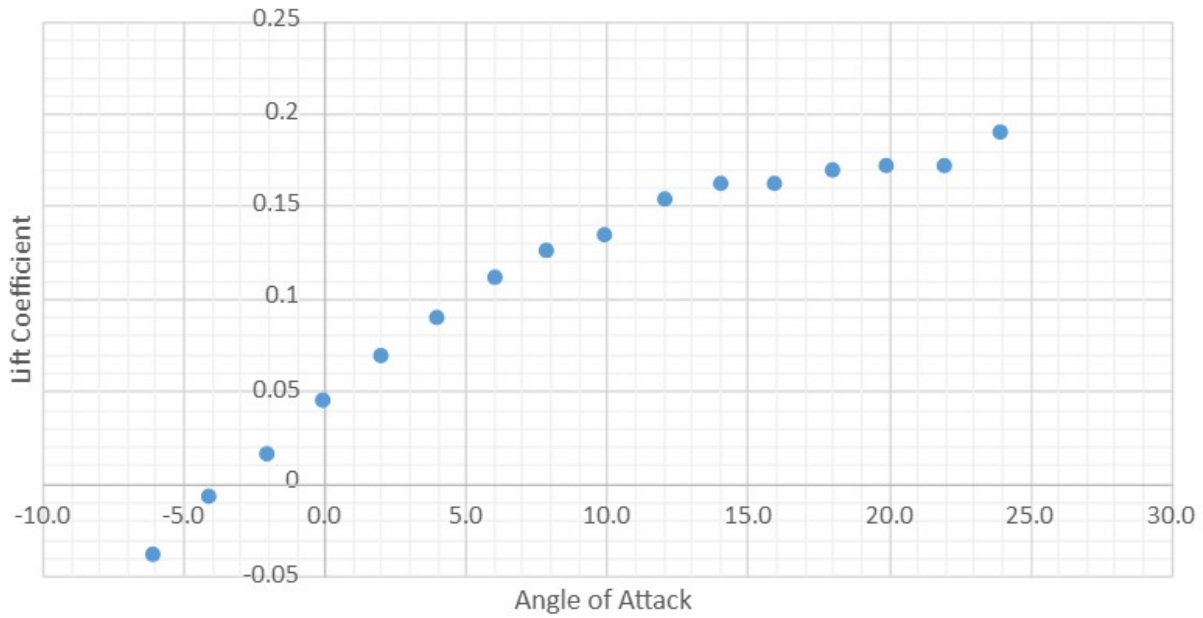


Fig. 12 Lift Coefficient with increasing Angle of Attack measured with a sting balance

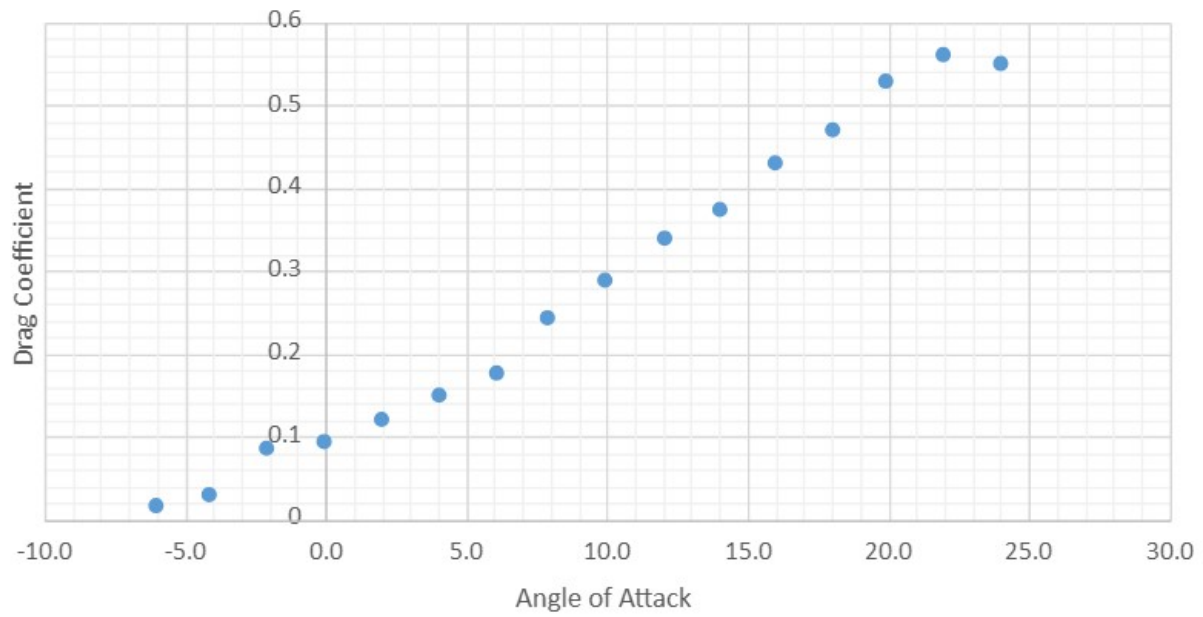


Fig. 13 Drag Coefficient with increasing Angle of Attack measured with a sting balance

E. Full-Scale Vehicle Dimensions and Payload

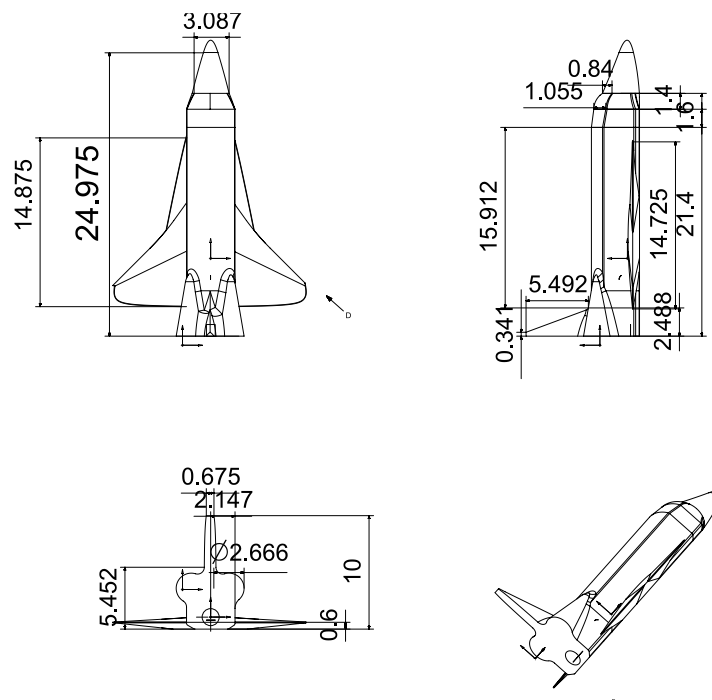


Fig. 14 Full Scale Model 3-View

Ideally, the addition of a 4 kg payload to the shuttle prototype should change the location of the center of gravity (CG) as little as possible. As such, the desired location for this payload would be on the CG, which, as mentioned previously, is located 3.3872 in from the aft end of the scaled-down model and 13.5488 in from the aft end of the full-scale prototype. A 4 kg, or 8.818 lb, payload placed here would change the aircraft weight, and therefore its lift-to-drag ratio (L/D) and glide angle, but not its CG and neutral point location.

According to Raymer [10], the equation for glide angle is given by:

$$\frac{L}{D} = \frac{1}{\tan(\gamma)} \quad (16)$$

Based on the $\frac{L}{D}_{\max}$ found previously, the glide angle, $\gamma = 56.94^\circ$.

This number makes sense because the shuttle wants a low L/D ratio to slow down during descent, which correlates with this relatively high glide angle. The re-entry vehicle was not meant to be a good glider.

With the addition of the 8.818 lb payload, the new $\frac{L}{D}_{\max}$ becomes:

$$\frac{0.5622}{0.7433_{\max}} = 0.756 = \frac{1}{\tan(\gamma)}$$

Then, $\gamma = 49.70^\circ$. Arguably, this is a more reasonable glide angle than without the payload.

The addition of the point mass would also increase the moment by a set amount, the distance from the CG to the moment balance multiplied by the point mass. By adding this moment to the recorded moment data, scaled up to the full sized prototype, the new moments look like the following:

Angle of Attack (deg)	Moment (Nm)
-6.0	0.103645
-4.1	0.105706
-2.1	0.108096
-0.1	0.110327
2.0	0.112105
4.0	0.114114
6.1	0.116147
7.9	0.118208
10.0	0.120688
12.1	0.123152
14.0	0.124744
16.0	0.126863
19.9	0.129445
22.0	0.134293
24.0	0.136500

Table 6 Angle of Attack vs. Moment Data

F. Static Stability Concerns

The longitudinal static stability of the aircraft is determined by the location of its neutral point. For an aircraft to be longitudinally statically stable, its neutral point must lie behind its center of gravity. The aircraft's center of gravity is located 3.3872 inches from its aft end. The neutral point, having been determined to be 2.472 inches from the tail in subsection V.D, lies 0.9152 inches behind the center of gravity in the aircraft's scaled down model. This distance between the center of gravity and neutral point is commonly known as the static margin.

G. Full-Scale Prototype Equivalent Mach Numbers

In this experiment, the model had $C_{root} = 4.84$ inches and $C_{tip} = 0.6$ inches. Using Equations 2a and 2b, this results with $\bar{C} = 0.126$ inches.

During the testing on the model, the velocities used for the three trials were 35 ft/sec, 55 ft/sec, and 75 ft/sec. Using Equation 1, this results in Reynolds numbers of 5.51e4, 8.93e4, and 1.22e5 respectively.

Next, Table 7 shows the equivalent Reynolds Numbers for the full-scale prototype corresponding to each of these Reynolds numbers for the model.

Re	V at 0 ft (ft/sec)	V at 30,000 ft (ft/sec)	V at 50,000 ft (ft/sec)	V at 70,000 ft (ft/sec)
5.51e4	8.74	19.5	45.4	119.4
8.993e4	13.8	30.6	71.5	187.8
1.22e5	18.7	41.6	97.3	255.6

Table 7 Equivalent Reynolds Numbers for the Full-Scale Prototype

It was decided that the equivalent velocities for these three Reynolds numbers encompassed the range of design velocities for the prototype. At these velocities, the prototype vehicle's exterior would need to be designed with materials designed to withstand very high temperatures.

VI. Experimental Uncertainty

A. 3-Component Sting Balance

The normal force measurement has a $\pm 5\%$ uncertainty of a full-scale value of 20 lbf, which results in an uncertainty of ± 1 lbf. The axial force measurement also has a $\pm 5\%$ uncertainty but of a full-scale value of 9 lbf, which results in an uncertainty of ± 0.45 lbf. Finally, the pitching moment measurement has an uncertainty of $\pm 5\%$ of a full scale value of 40 in-lbf, resulting in an uncertainty of ± 2 in-lbf.

B. Omega PX653 Pressure Transmitter

The uncertainty present in the analyses for this lab are due to the transducers used to measure the ambient pressure, ambient temperature and the dynamic pressure. The ambient pressure and temperature, measured with the *Compact Digital Barometer*, are expected to have uncertainties of ± 0.148 Hg and $\pm 1.8^\circ F$ respectively. The dynamic pressure, measured with the *PSI Netscanner Pressure System*, can be expected to have an uncertainty of $\pm 0.1\%$ of the full scale value (0.001 psi).

C. Model Positioning System

The measurement of the angle of attack of the model has an uncertainty of $\pm 0.2^\circ$. Additionally, if the angle of attack was mistakenly increased too much and subsequently corrected, significant error may have come from the boundary layer being affected at the higher angle.

VII. Conclusion

Through this lab, the aerodynamic performance of a CubeSat recovery vehicle was analyzed to support the design of the vehicle as well as demonstrate its capability to perform well under the expected conditions. Through the lab results, it can be seen that the design of the vehicle can be expected to perform well in expected conditions as the aerodynamic performance of the 1/4 scale model succeeded in the wind tunnel. Through the simulation of the smaller scale model in a low-speed wind tunnel, the recovery vehicle's lift, drag, and pitching moment were able to be calculated which gives insight into its performance at 70,000 ft. The neutral point of 2.472 inches from the aft shows the design is longitudinally stable, while the center of gravity of 3.3872 inches from the aft shows the vehicle's stability in flight. The calculated lift to drag ratio with a payload of 8.818 lbs was 0.756 corresponding to a glide angle of 49.70° . Despite the glide angle being relatively steep, this proves to be helpful as the vehicle is set to safely and efficiently return payloads back to Earth from high altitudes. The aerodynamic performance of the scaled model shows the vehicle's capabilities to succeed even in the expected conditions.

The Aerolab low-speed wind tunnel has an operational range of 10–145 mph, which is insufficient for testing the recovery vehicle as it operates at significantly higher speeds. Additionally, the wind tunnel's test section, measuring 12" \times 12" \times 24", necessitates the use of a 1/4-scale model to minimize wall effects. This experiment could be conducted in a more advanced wind tunnel with a larger test section and higher operational speed. Furthermore, a test model built using similar materials as the actual recovery vehicle would give results that's more feasible compare to the ones generated using 3D printed model.

References

- [1] "Experiment #5: Design Lab," *AE 460: Aerodynamics & Propulsion Laboratory*, Department of Aerospace Engineering, University of Illinois at Urban-Champaign.
- [2] NASA, "What Are Smallsats and CubeSats?" NASA, <https://www.nasa.gov/what-are-smallsats-and-cubesats/>. Accessed 11 Dec. 2024.
- [3] Aksoy, M., "CubeSats: Tiny Satellites Are Changing How We Explore the Solar System," Space.com, Oct. 15, 2024. <https://www.space.com/cubesats-changing-how-we-explore-the-solar-system>. Accessed 11 Dec. 2024.
- [4] SpaceWorks Enterprises, Inc., "RED-Data Capsule," SpaceWorks, <https://www.spaceworks.aero/defense-space/entry-systems/red-data/#red-data>. Accessed 11 Dec. 2024.
- [5] Saeed, N., Elzanaty, A., Almorad, H., Dahrouj, H., Al-Naffouri, T. Y., and Alouini, M.-S., "CubeSat Communications: Recent Advances and Future Challenges," *IEEE Communications Surveys & Tutorials*, Vol. 22, No. 3, 2020, pp. 1839–1862. <https://doi.org/10.1109/COMST.2020.2990499>.
- [6] Vergun, D., "Nanosatellites Could Play Pivotal Role in Defense Against Enemy Missiles," DOD News, U.S. Department of Defense, <https://www.defense.gov/News/News-Stories/Article/Article/2685840/nanosatellites-could-play-pivotal-role-in-defense-against-enemy-missiles/>. Accessed 11 Dec. 2024.
- [8] NASA Jet Propulsion Laboratory, "CubeSats," JPL, <https://www.jpl.nasa.gov/topics/cubesats/>. Accessed 11 Dec. 2024.
- [9] Villela, T., Costa, C. A., Brandão, A. M., Bueno, F. T., and Leonardi, R., "Towards the Thousandth CubeSat: A Statistical Overview," *International Journal of Aerospace Engineering*, first published 10 Jan. 2019. <https://doi.org/10.1155/2019/5063145>.
- [10] Raymer, D., *Aircraft Design: A Conceptual Approach*, 6th Edition, AIAA Inc., Reston, VA, 2012.
- [11] United States, *U.S. Standard Atmosphere, 1962: ICAO Standard Atmosphere to 20 Kilometers, Proposed ICAO Extension to 32 Kilometers, Tables and Data to 700 Kilometers*, Headquarters, December 1962.
- [12] United States, *U.S. Standard Atmosphere, 1976*, Technical Memorandum NOAA-S/T-76-1562, NASA-TM-X-74335, October 1976.

Appendix A: Sample Calculations

A. Reynolds Number

$$\lambda = \frac{0.6in}{4.76in} = 0.126 \quad (17a)$$

$$\bar{c} = \frac{2}{3}(4.76in) \frac{1 + 0.126 + 0.126^2}{1 + 0.126} = 3.27in \quad (17b)$$

$$Re = \frac{(2.216E - 3slug/ft^3)(35ft/sec)(3.27inches)(1ft/12inches)}{(3.852e - 7slug/ft - s)} = 5.49e - 4 \quad (17c)$$

B. Total Normal and Axial Force

$$N_{total} = (-0.0977lbf) + (2.77lbf)\cos(-6^\circ) = 2.65lbf \quad (18a)$$

$$A_{total} = -0.00236 - (2.77lbf)\sin(-6^\circ) = 0.288lbf \quad (18b)$$

C. Lift and Drag

$$L = (2.65lbf)\cos(-6^\circ) - (0.288lbf)\sin(-6^\circ) = 2.61lbf \quad (19a)$$

$$D = (2.65lbf)\sin(-6^\circ) + (0.288lbf)\cos(-6^\circ) = 0.566lbf \quad (19b)$$

$$C_L = \frac{2.61lbf}{\frac{1}{2}(2.216E - 3slug/ft^3)(35ft/sec)^2S} \quad (20a)$$

$$C_D = \frac{0.566lbf}{\frac{1}{2}(2.216E - 3slug/ft^3)(35ft/sec)^2S} \quad (20b)$$

D. Moment about Neutral Point

$$M_{np} = (-0.0771in*lbf) - (2.65lb)(0.0628inches - 0.32inches) + (0.288lbf)(3.39inches - 0.32inches) = 0.795in*lbf \quad (21)$$

E. Glide Angle

$$\frac{L}{D} = \frac{1}{\tan(\gamma)}$$

$$\frac{0.258}{0.743} = \frac{1}{\tan(\gamma)}$$

$$0.347 \approx \frac{1}{\tan(\gamma)}$$

$$\gamma \approx 56.94^\circ$$

Appendix B: Raw Data

Data Point	alpha [deg]	Normal Force [lbf]	Axial Force [lbf]	Pitching Moment [in-lbf]	Velocity [ft/s]	Reynolds Number
1	-6.03	-0.1	0	-0.08	35.01	54882.5
2	-4.11	-0.09	0	-0.06	35.22	55212.2
3	-2.06	-0.08	0.02	-0.04	35.07	54908.7
4	0.06	-0.07	0.03	-0.02	34.98	54842.8
5	2.02	-0.06	0.04	0	35.51	55668
6	4.01	-0.06	0.05	0.01	35.32	55369.9
7	6.07	-0.05	0.06	0.03	35.04	54928.4
8	7.9	-0.04	0.08	0.05	35.06	54962.8
9	9.97	-0.03	0.09	0.08	35.17	55131.7
10	12.08	-0.02	0.11	0.1	35.39	55478.2
11	14.02	-0.01	0.12	0.12	35.1	55019.1
12	16	0	0.13	0.15	35.09	55013.3
13	18.01	0.01	0.14	0.17	35.05	54949.4
14	19.94	0.02	0.16	0.2	34.83	54599.6
15	22	0.03	0.17	0.23	35.12	55054.4
16	24	0.04	0.16	0.25	35.28	55310.8

Table 8 Raw Data for $R_e = 5.51e4$

Appendix C: Group Member Participation

Group Member	Contribution to Technical Note
--------------	--------------------------------

William Boer	Contributed to the theory, results and appendix section
Aden Litwiller	Wrote Theory and Analysis
Justin Magsino	Authored the conclusion, simple theoretical analysis of the expected performance, and contributed to results
Amber Miller	Contributed to the theory, results and appendix section
Musong Qin	Authored the abstract, introduction, apparatus, procedure and uncertainty analysis